Spin Relaxation and Lifetime in Fe/GaAs Heterostructures at Low Temperatures

A THESIS
SUBMITTED TO THE FACULTY OF THE GRADUATE SCHOOL
OF THE UNIVERSITY OF MINNESOTA
BY

Juan Carlos Tigre Lazo

IN PARTIAL FULFILLMENT OF THE REQUIREMENTS
FOR THE DEGREE OF
MASTER OF SCIENCE

Paul Crowell

July, 2019

Acknowledgements

I would like to extend my sincere gratitude to the people that made this work possible. I am deeply indebted to Professor Paul Crowell for all his valuable advice and support. Thanks also to Zhen Jiang for his patience and assistance.

Dedication

To my parents

Abstract

In the research reported in this thesis, the spin properties of an Fe/n-GaAs lateral spin valve were studied. Of special interest in the study of spin dynamics in semiconductors is determining sources of spin relaxation at low temperatures and distinguishing their range. The goal of this paper is to extend current knowledge of electron spin relaxation and lifetime τ_s at sub-40 K temperatures in Fe/n-GaAs spin valves, employing a pump-probe measurement scheme to remove hyperfine effects.

Chapter 1 begins with an overview of the study of τ_s in n-GaAs. The relevant spin relaxation mechanisms at low temperatures are laid out as well as the spin transport theory. Chapter 2 describes the charge transport properties of the sample studied and the standard measurement techniques to be used in this paper. In Chapter 3, spin valve results and Hanle data are examined to determine τ_s and diffusion coefficients. Diffusion coefficients are determined using the standard 1D lateral spin drift-diffusion model as well as transport measurements. Chapter 4 looks at the temperature dependence of the τ_s and compares results to published work.

In particular, τ_s values obtained from 1-parameter and 2-parameter fitting of Hanle data are in agreement and indicate τ_s continues to increase below T = 20 K. Current pulsing is also shown to remove any visible Dynamic Nuclear Polarization (DNP) signatures down to T = 2 K. The spin relaxation rate below 40 K is not found to be consistent with D'yakonov-Perel' or Elliot-Yafet relaxation. Furthermore, differences in τ_s values between similarly doped n-GaAs spin valves are observed and could be explained by complications inherent to the τ_s measurement schemes.

Contents

List of Figures

Chapter 1

Introduction

1.1 Background

Experiments by Tedrow and Meservey in the 1970's showed that passing a current across a ferromagnet (FM)/insulator/superconductor junction creates spin-polarized current that persists even outside the FM region [1]. It was also shown by Julliere in FM/I/FM structures that the conductance value depends on the relative FM orientations, which can be toggled by applying an external magnetic field [2]. Then in 1985, experiments by Johnson and Silsbee demonstrated spin accumulation and precession in metals up to 77 K [3]. In l988, Albert Fert and Peter Grunberg discovered Giant Magnetoresistance (GMR), which occurs by layering FM and ordinary metallic materials. This result has been extensively used for nonvolatile memory applications [4]. Since then, a wave of research focused on the manipulation of spin in metals and semiconductors (SCs) for device applications began. To develop these spin-based electronic (spintronic) devices, a working understanding of spin-resolved transport phenomena in different materials is needed. One of the goals of spintronics research is to find materials that allow for spin injection, manipulation, and detection well above room temperature, at length scales comparable to current electronic devices. Towards this goal, much research has been done in ordinary metals, ferromagnets, SCs, non-magnetic materials, etc. at T near room temperature. However, our understanding of spin relaxation mechanisms that affect the spin lifetime τ_s for temperatures below 40 K is not as good.

Theoretical "phase" diagrams constructed by Song and Kim (2002) indicate that for most n-doped III-V SC (including GaAs) below T = 5 K the relevant spin relaxation mechanism is Elliot-Yafet (EY). Above this temperature the D'yakonov-Perel' (DP) spin relaxation mechanism is dominant. This result is claimed to hold for $n = 10^{14}$ cm$^{-3} - 10^{20}$ cm^{-3}. In their calculations, however, they used classical Boltzmann statistics for determining the momentum relaxation time τ_p and neglected nuclear-electron hyperfine interactions.

Dzhioev *et.al.* (2002) compiled τ_s results from many experiments on n-GaAs for $n = 10^{15}$ cm$^{-3} - 10^{19}$ cm^{-3} and temperatures between 2 K and 5 K. It was found that the dominant spin relaxation mechanism for densities above the metal-insulator transition (MIT), known to be 2×10^{16} cm^{-3} for GaAs, was DP for this temperature range. Below the MIT, anisotropic exchange relaxation, and then relaxation due to the hyperfine interaction, dominates. The consensus based on recent measurements [5][6][7][8] is that for n-GaAs doped near the MIT, DP dominates above 40 K. Below 40 K, the measured τ_s in these experiments tend to fall below the values predicted by DP relaxation, indicative of a stronger relaxation mechanism taking place. The goal of this research is to better identify the different spin relaxation mechanisms at temperatures below 40 K. This will be done using an Fe/n-GaAs spin valve, which has proven to be very useful in studying spin transport in III-V SCs.

1.2 Spin Valve

Spin valves are devices that can toggle between two electrical resistance states, analogous to how a transistor acts as a switch. A spin valve can be formed by sandwiching a non-magnetic material between two conducting materials, usually FMs. The resistance across the device can have a higher or lower value, depending on the relative orientation of the magnetizations of the FMs.

Spin valves serve as a test bed for possible spintronic devices. One such device is a

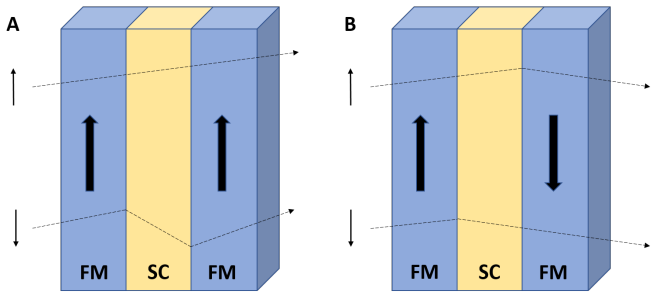

Figure 1.1: Illustration of a spin valve formed using two ferromagnetic materials (FM) separated by a semiconductor spacer layer (SC) in the parallel (A) and antiparallel (B) configuration. Dashed lines represent spin trajectories and thick black arrows represent FM magnetization orientations. In the antiparallel configuration there is a greater spin backscattering probability, resulting in higher resistance.

spin-valve transistor, which acts much like a bipolar transistor and has the typical emitter/base/collector structure [9]. In order to build spin based devices, non-equilibrium spin accumulations must be created, manipulated, and detected well above room temperature. Spin lifetimes must also be long enough to allow for large steady-state spin accumulations. All-electrical, all-SC room temperature spin valves have been pursued for over a decade, as they could be easily incorporated into integrated circuits, but overcoming low spin injection efficiencies and large spin relaxation without using magnetic or optical components is no easy task [10]. However, much progress in the understanding of spin dynamics has been made through the use of spin valves with FM contacts.

n-doped GaAs based spin valves have been used in the past to study the spin properties of new device combinations, using both optical and electrical means. Very high electron mobilities and wide temperature operating ranges make GaAs a promising candidate for many technological applications. GaAs is also a direct bandgap SC, making it relevant for opto-electronic applications as well. Of special importance are the electron spin characteristics of GaAs at various doping and temperature ranges for use in spintronic devices. Hence, understanding the electron spin dynamics in GaAs is imperative to the development of future spin-based devices. When GaAs is used in spin valves, it is usually doped near the metal-insulator transition (MIT) in order to maximize the spin lifetime. To achieve large spin injection efficiencies, FM injector and detector contacts

are used. To reduce the backflow of injected electron spins, Schottky barriers are created using modulation doping.

1.3 Spin Injection and Detection

When a current is applied across the interface between a FM and a SC, a spin current will exist due to the large imbalance of spin bands at the Fermi surface of the FM. This results in a net polarized current,

$$I_m = \frac{\eta \mu_B I_e}{e}, \tag{1.1}$$

to be injected into the SC, where η is a phenomenological constant for the spin injection efficiency, μ_B is the Bohr magneton, and I_e is the applied electric current. The polarization of the injected current will be pararllel or anti-parallel to the magnetization of the ferromagnet. The injected spins will diffuse a distance $\lambda_s = \sqrt{D\tau_s}$, where λ_s is the diffusion length, D is the spin diffusion constant, and τ_s is the spin lifetime, before decaying due to spin-relaxation mechanisms. Residual non-equilibrium spin accumulation away from the injector contact can be measured as a voltage signal.

1.4 Lateral Spin Valve

A lateral spin valve can be made by placing ferromagnetic (FM) contacts on a SC, such as GaAs. These contacts are used to inject and detect non-equilibrium spin accumulation in the GaAs channel. Spin current is injected from the FM contact into the SC by applying a charge current across the interface. Spins will diffuse outward from the injection site and can be measured as a voltage signal across the detector interface. This voltage is proportional to the net spin polarization in the SC at the detector and the sensitivity of the FM contacts [3]. In the non-local spin valve (NLSV) configuration, shown in Figure 1.2, spin detection is accomplished using FM contacts that lie outside the charge current path.

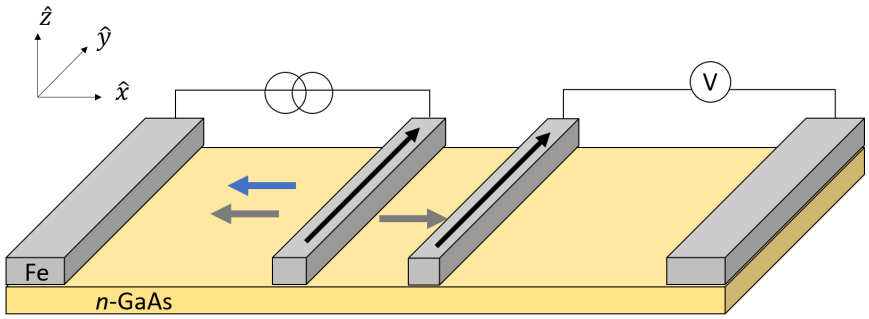

Figure 1.2: Lateral non-local spin valve. Fe contacts are shown in gray and n-GaAs in yellow. The blue arrow indicates the charge path and grey arrows indicate the spin diffusion path.

This setup is different than the three-terminal measurement geometry where a center electrode is used for both injection and detection. The non-local setup helps reduce unwanted contributions from ohmic resistance, fringe fields, anisotropic magnetoresistances, and local Hall effects.

A spin-valve signal can be generated by sweeping an in-plane magnetic field (B_y), causing the relative contact magnetizations to switch, resulting in a change in the detection voltage. Figure 1.3 shows a Fe/n-GaAs NLSV signal at 30 K. The center feature is due to the hyperfine interaction between electrons and nuclei in GaAs. At low external fields, an internal magnetic field B_n, resulting from polarized nuclei, causes spin dephasing, suppressing the spin signal. We will return to this topic later in this thesis.

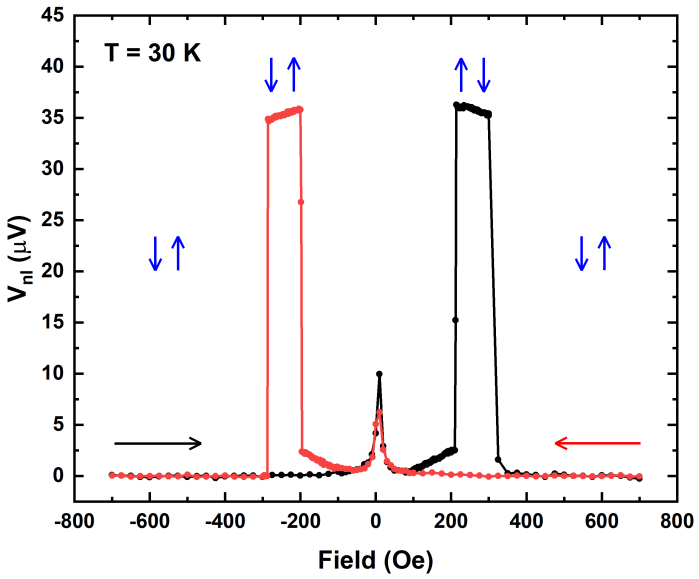

Figure 1.3: Fe/n-GaAs NLSV signal at 30 K. Red and black arrows indicate B_y field sweep direction. Blue arrows indicate FM injector and detector magnetization directions.

1.5 Hanle Effect

The Hanle effect describes spin precession inside semiconductors when a magnetic field is applied perpendicular to the spin injection direction. This effect is considered a hallmark of a spin signal and is useful in determining spin properties of materials.

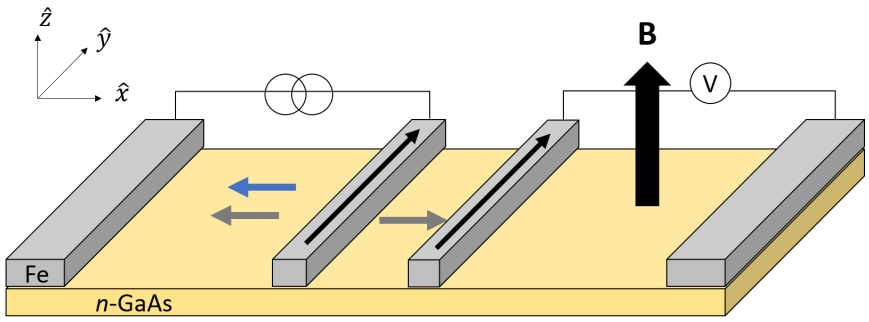

Figure 1.4: Setup for Hanle Measurements.

As injected spins diffuse outward from the injection site, they precess about the perpendicular field. Different paths will result in different travel times and Larmor phases, causing the spins to dephase and randomize. The measured voltage signal is proportional to the remnant spin polarization at the detector, projected along the detector magnetization direction,

$$V \propto \mathbf{P} \cdot \hat{\mathbf{m}}_{FM}. \tag{1.2}$$

A Hanle signal is obtained by sweeping an out-of-plane external field (B_z) and measuring the non-local voltage. This is done for both the parallel and antiparallel FM contact polarization directions. Figure 1.5 shows a sample Hanle curve of an Fe/n-GaAs non-local spin valve at 30 K.

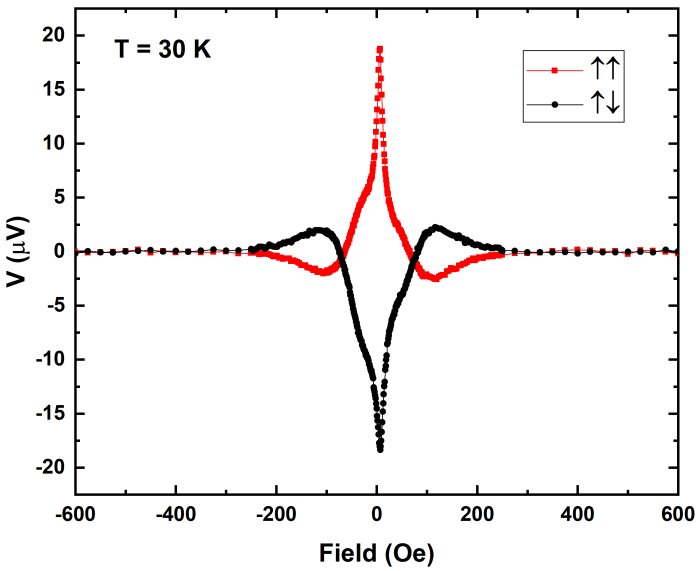

Figure 1.5: NLSV signal vs B_z (Hanle curve).

The voltage difference between the parallel and anti-parallel injector and detector configurations (Figure 1.6) will give the non-local voltage signal,

$$V_{nl} = V_{\uparrow\uparrow} - V_{\uparrow\downarrow}. \tag{1.3}$$

As shown in Figure 1.7, both NLSV and Hanle measurements should indicate the same magnitude of the non-local voltage signal. Characteristic of Hanle spin signals is the Lorentzian line shape, demonstrating maximum spin polarization at the detector electrode when no out-of-plane magnetic field is applied, followed by symmetrical dips in the signal due to the average spin precessing into an anti-parallel orientation to the detector electrode polarization. For large enough fields, $\omega_L \tau_s \gg 1$, where $\omega_L = -\gamma_e B$ is the Larmor frequency and γ_e is the gyromagnetic ratio, suppression of the Hanle signal occurs due to sufficient decoherence of spins. At low fields, where the nuclear Overhausser field is comparable to the external field, spin relaxation occurs from precession about B_n, suppressing the spin signal.

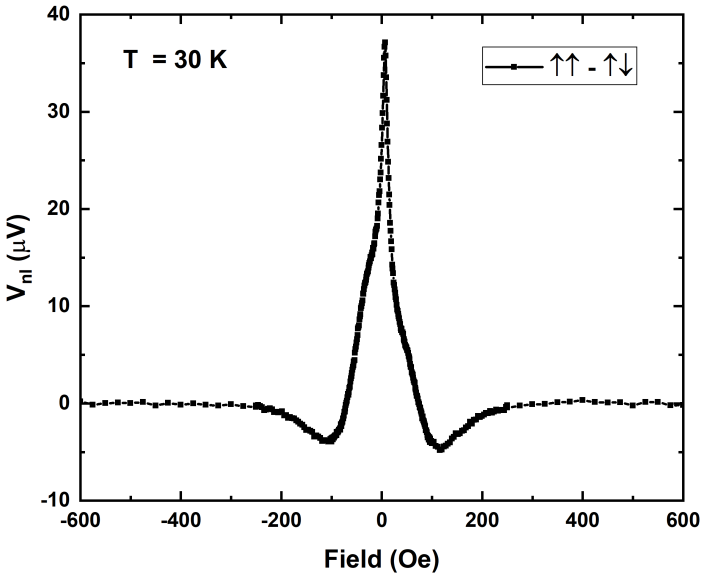

Figure 1.6: NLSV voltage signal difference between parallel and antiparallel FM contact orientation.

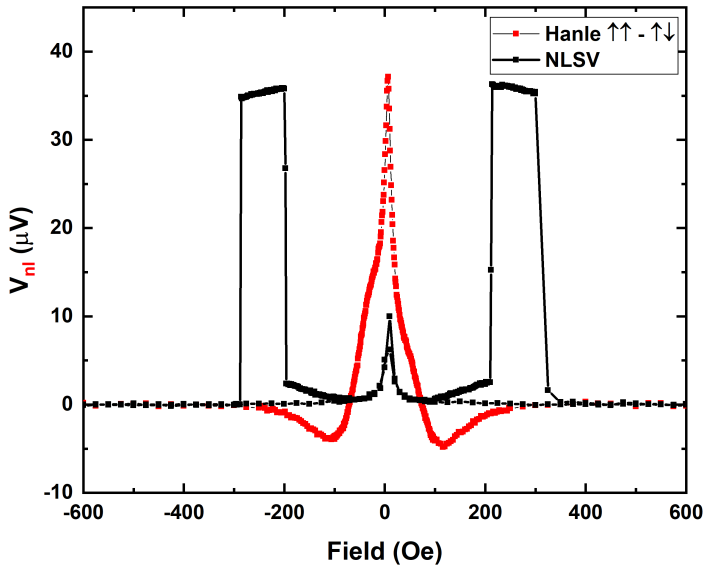

Figure 1.7: Overlay of non-local spin valve and Hanle signal. The Hanle signal was obtained from subtracting the antiparallel voltage signal from the parallel one. The voltage signal corresponds to the spin polarization at the detector.

1.6 Theory

The theory necessary for understanding the Hanle signal will now be introduced using the approach of Yu and Flatté [11].

Lateral Drift Diffusion Model

The lateral drift-diffusion model is derived, focusing on spin polarization outside of the charge path. The current for spin ↑ (↓) electrons can be written as

$$\mathbf{j}_{\uparrow(\downarrow)} = \sigma_{\uparrow(\downarrow)}\mathbf{E} - eD_{\uparrow(\downarrow)}\nabla n_{\uparrow(\downarrow)}, \tag{1.4}$$

where ↑ (↓) is the projection of the electron spin direction along an axis, σ is the spin channel conductivity, D is the diffusion coefficient, and n is the spin density. Equation 1.4 states that a spin current will arise due to drift under an electric field as well as diffusion. The continuity equation, modified to include relaxation, for spin up electron density is

$$\frac{\partial n_\uparrow}{\partial t} + \frac{1}{(-e)}\nabla \cdot j_\uparrow = -\frac{n_\uparrow}{\tau_{\uparrow\downarrow}} + \frac{n_\downarrow}{\tau_{\downarrow\uparrow}}, \tag{1.5}$$

where $\tau_{\uparrow\downarrow}^{-1}$ ($\tau_{\downarrow\uparrow}^{-1}$) represents the rate at which spin ↑ (↓) electrons flip. Using Equations 1.4, 1.5, the drift-diffusion equations for spin up and spin down electrons can be written as

$$\frac{\partial n_\uparrow}{\partial t} + \frac{1}{(-e)}\nabla\sigma_\uparrow \cdot \mathbf{E} + \frac{1}{(-e)}\sigma_\uparrow \nabla \cdot \mathbf{E} - D_\uparrow \nabla^2 n_\uparrow = -\frac{n_\uparrow}{\tau_{\uparrow\downarrow}} + \frac{n_\downarrow}{\tau_{\downarrow\uparrow}}; \tag{1.6}$$

$$\frac{\partial n_\downarrow}{\partial t} + \frac{1}{(-e)}\nabla\sigma_\downarrow \cdot \mathbf{E} + \frac{1}{(-e)}\sigma_\downarrow \nabla \cdot \mathbf{E} - D_\downarrow \nabla^2 n_\downarrow = -\frac{n_\downarrow}{\tau_{\downarrow\uparrow}} + \frac{n_\uparrow}{\tau_{\uparrow\downarrow}}. \tag{1.7}$$

In non-magnetic materials, which are the focus of this work, $D_\uparrow = D_\downarrow$ and the mobility $\nu_\uparrow = \frac{\sigma_\uparrow}{n_\uparrow e} = \nu_\downarrow$ (assuming spatially uniform conductivity). In doped semiconductors, we assume thus,

$$\frac{1}{n_\uparrow} = -\frac{1}{n_\downarrow}. \tag{1.8}$$

Using local charge neutrality, subtracting Equation 1.6 from Equation 1.7, and considering only regimes without electric fields, we obtain the spin diffusion equation,

$$\frac{\partial(n_\uparrow - n_\downarrow)}{\partial t} - D\nabla^2(n_\uparrow - n_\downarrow) = -\frac{n_\uparrow - n_\downarrow}{\tau_s}, \tag{1.9}$$

where $(\tau_s)^{-1} = (\tau_{\uparrow\downarrow})^{-1} + (\tau_{\downarrow\uparrow})^{-1}$ is the spin lifetime.

The spin polarization is defined as

$$P = \frac{n_\uparrow - n_\downarrow}{n_\uparrow + n_\downarrow}. \tag{1.10}$$

Simplifying Equation 1.9

$$\frac{\partial P}{\partial t} = D\nabla^2 P - \frac{P}{\tau_s}. \tag{1.11}$$

Precession will occur in the case of an applied field perpendicular to the injected spin polarization, as shown in Figure 1.4,

$$\left(\frac{\partial \mathbf{P}}{\partial t}\right)_{precess} = -\gamma_e \mathbf{B} \times \mathbf{P}, \tag{1.12}$$

where γ_e is the gyromagnetic ratio. The motion of the polarization in the plane perpendicular to the magnetic field may be mapped onto the complex plane, $P = P_x + iP_y$, such that for spin polarization in the y direction the Larmor precession term simplifies to,

$$\left(\frac{\partial P}{\partial t}\right)_{precess} = -i\gamma_e BP. \tag{1.13}$$

The spin current injected from the FM contact into the SC can be defined as,

$$j_s = j_\uparrow - j_\downarrow. \tag{1.14}$$

The polarized current injected from FM contact into the SC channel can be defined as

$$\frac{j_s^0}{neD}\delta(x), \tag{1.15}$$

where j_s^0 is the initial injected spin current and $\delta(x)$ is due to representing the source as a point in 1D. Combining Equations 1.11, 1.13, 1.15, the dynamics of the polarization along the direction of the injected spin polarization are governed by,

$$\nabla^2 P = \frac{P}{D\tau_s} + \frac{i\gamma_e BP}{D} + \frac{j_s^0}{neD}\delta(x) = \frac{P}{\lambda^2} + \frac{j_s^0}{neD}\delta(x). \tag{1.16}$$

The terms linear in P can be combined to give an effective complex spin diffusion length, $\lambda = \sqrt{\frac{D\tau_s}{1+i\gamma_e B\tau_s}}$. The solution to this equation to the right of the contact ($x > 0$) is given by

$$P = Ce^{-x/\lambda} - \frac{j_s^0\lambda}{2neD}e^{-x/\lambda}. \tag{1.17}$$

The injected spin current can be related to the spin density difference using Equation 1.4,

$$j_s^0 = -eD\nabla(n_\uparrow - n_\downarrow), \tag{1.18}$$

and the polarization using Equation 1.10,

$$-\frac{j_s^0\tau_s}{ne\lambda_s^2} = \nabla P. \tag{1.19}$$

Then Equation 1.17 can be used with Equation 1.19 and evaluated at the injector to find the constant of integration. This yields the spin polarization in the semiconductor,

$$P_{SC} = \alpha\frac{j_s^0\lambda}{neD}e^{-x/\lambda}, \tag{1.20}$$

where α is a phenomenological constant accounting for the detection efficiency. Using

the fact that $j_s^0 = \eta P_{FM} j_e$, where η is the injection efficiency, P_{FM} is the FM contact spin polarization and $j_e = j_\uparrow + j_\downarrow$ is the charge current,

$$P_{SC} = \frac{\alpha \eta P_{FM} j_e \lambda}{neD} e^{-x/\lambda}. \tag{1.21}$$

The electrochemical potential for a spin species β is defined as

$$\zeta_\beta = \frac{\partial F(\mu_{n_\uparrow}, \mu_{n_\downarrow})}{\partial n_\beta} - e\phi(x), \tag{1.22}$$

where $\mu_\beta = \frac{\partial F(\mu_{n_\uparrow}, \mu_{n_\downarrow})}{\partial n_\beta}$ is the chemical potential, F is the local free energy density, and $\phi(x)$ is the electrostatic potential. At the FM/N detector interface, in the presence of a current, the spin-resolved electro-chemical potentials are discontinuous and the junction is a spin-selective resistive interface. By measuring a voltage signal one is probing the chemical potential corresponding to the FM contact magnetization direction. The potential difference between the parallel and antiparallel FM contact orientations is given by

$$V_{nl} = V_{\uparrow\uparrow} - V_{\downarrow\uparrow} = \frac{P_{FM}}{-e}(\mu_\uparrow - \mu_\downarrow). \tag{1.23}$$

In the limit where $\mu_\uparrow - \mu_\downarrow \ll \epsilon_F$,

$$\mu_\uparrow - \mu_\downarrow = \frac{n_\uparrow - n_\downarrow}{N_{3D}(\epsilon_F)}, \tag{1.24}$$

where $N_{3D}(\epsilon_F)$ is the density of states at the Fermi energy ϵ_F in the semiconductor. The voltage signal measured at the detector that results from switching the relative orientation of the ferromagnets is given by,

$$V_{nl} = -\frac{P_{FM}}{e}\frac{n_\uparrow - n_\downarrow}{N_{3D}(\epsilon_F)} n P_{SC} = -\frac{I}{A}\frac{\lambda}{\sigma}\eta\alpha(P_{FM})^2 e^{-x/\lambda}, \tag{1.25}$$

where $\sigma = e^2 N_{3D}(\epsilon_F) D$ is the semiconductor conductivity. Approximating the dispersion relation as parabolic,

$$N_{3D}(\epsilon_F) = \frac{8\sqrt{2}}{h^3} \pi m^{*3/2} (\epsilon_F)^{1/2}. \tag{1.26}$$

Thus, the voltage signal measured at the detector that results from switching the relative orientation of the ferromagnets is given by

$$V_{nl} = -\frac{P_{FM}}{e} \frac{n_\uparrow - n_\downarrow}{\frac{3}{2}\frac{n}{\epsilon_F}} = -\frac{2}{3e} P_{FM} P_{SC} \epsilon_F = -\frac{2}{3} \frac{I \lambda \epsilon_F}{A n e^2 D} \eta \alpha (P_{FM})^2 e^{-x/\lambda}, \tag{1.27}$$

where P_{Fe} is the injector polarization and P_{SC} is the semiconductor polarization at the detector.

1.7 Diffusion Coefficient

The diffusion coefficient of carriers inside the semiconductor can be determined from the Einstein relation [12]

$$D = \frac{n\nu}{e} \left(\frac{\partial \mu}{\partial n} \right), \tag{1.28}$$

where ν is the mobility and $\frac{\partial \mu}{\partial n}$ is the inverse electronic compressibility, which is calculated by

$$\left(\frac{\partial \mu}{\partial n} \right) = \frac{k_B T}{n} \frac{F_{\frac{1}{2}}(\xi)}{F_{-\frac{1}{2}}(\xi)}, \tag{1.29}$$

where $\xi = \frac{\mu}{k_B T}$ is the reduced chemical potential and F is the complete Fermi-Dirac integral

$$F_\alpha(\zeta) = \frac{1}{\Gamma(\alpha + 1)} \int_0^\infty \frac{x^\alpha dx}{e^{x-\zeta} + 1}, \tag{1.30}$$

where $\Gamma(x)$ is the gamma function. In 1D, using the Sommerfield Expansion, μ at low temperatures can be approximated by

$$\mu = \epsilon_F \left[1 + \frac{\pi^2}{12}(\frac{k_b T}{\epsilon_F})^2\right] \approx \epsilon_F. \tag{1.31}$$

Utilizing the parabolic dispersion relation approximation to determine ϵ_F and obtaining ν from transport measurements, D can be obtained by

$$D = 2\frac{\nu}{e}k_B T \left(\int_0^\infty \frac{x^{\frac{1}{2}}dx}{e^{x-\frac{\epsilon_F}{k_B T}}+1}\right) / \left(\int_0^\infty \frac{x^{-\frac{1}{2}}dx}{e^{x-\frac{\epsilon_F}{k_B T}}+1}\right). \tag{1.32}$$

In the degenerate ($T \ll T_F$) and non-degenerate ($T \gg T_F$) limits, Equation 1.28 simplifies to [11]

$$D = \begin{cases} \frac{2}{3}\frac{\nu}{e}\epsilon_F, & \text{for } T \ll T_F, \quad (1.33a) \\ \frac{\nu}{e}k_B T, & \text{for } T \gg T_F. \quad (1.33b) \end{cases}$$

1.8 Spin Relaxation

The relevant spin relaxation mechanisms for n-doped, III-V semiconductors are the Elliot-Yafet (EY) and D'yakonov-Perel' (DP) relaxation mechanisms. These mechanisms emerge from the spin-orbit (SO) interaction. The hyperfine interaction can also result in spin relaxation at low temperatures.

In the Zeeman interaction, electrons, with spin quantum number $s = \frac{1}{2}$ and spin magnetic moment $\mu_s = -\mu_B \frac{g_s}{\hbar} S$, can couple to external magnetic fields with the Hamiltonian

$$H_z = \mu_B \frac{g_s}{\hbar} \mathbf{S} \cdot \mathbf{B}, \tag{1.34}$$

where g_s is the electron g-factor with a value of -0.44 at the conduction band edge of

GaAs. The Zeeman interaction energetically separates the electron spin states, providing access to the spin environment through the use of a magnetic field.

The hyperfine interaction describes the coupling of an electron's spin and angular momentum with a nuclear spin momentum I_n

$$H_{hf} = \Sigma_n C V_0 |\Psi(\mathbf{R_n})|^2 \hat{\mathbf{S}} \cdot \hat{\mathbf{I}}_\mathbf{n}, \tag{1.35}$$

where the sum is done over all nuclear sites R_n, C is the coupling constant and V_0 is the unit cell volume. However, due to the interaction requiring an overlap of the electron wavefunction with the nuclear magnetic moment, mostly S-wave eigenstates which contain negligible angular momentum, are involved. The interaction between nuclear moments and electrons allows for large nuclear polarization if the electron spin system is continuously pumped out of equilibrium. This process is known as dynamic nuclear polarization (DNP).

The SO interaction is the main source of spin relaxation in semiconductors. Inside a semiconductor, an electron's spin can couple to the potential landscape $V(\mathbf{r})$ given by the crystal lattice, defects, and external potentials. Electrons moving with momentum, $\mathbf{P} = \hbar\mathbf{k}$, feel the influence of an effective magnetic field, $\mathbf{B}_i = \frac{m}{e\hbar}\Omega(\mathbf{k})$, which can be described by the Hamiltonian

$$H_{SO} = \frac{1}{2}\mathbf{\Omega} \cdot \sigma, \tag{1.36}$$

where σ are the Pauli spin matrices and $\Omega(\mathbf{k})$ is a precession vector that reflects the lattice potential symmetry [13].

The EY mechanism results from the mixing of up and down spin states due to the SO interaction. As a result of this mixing, any spin-independent scattering can cause spin flips and thus relaxation. Characteristic of the EY mechanism is the dependence of τ_s on the momentum scattering time

$$\tau_s \propto \tau_p, \tag{1.37}$$

where the strength of this mechanism depends on the SO-splitting and the semiconductor band gap.

For materials lacking bulk inversion symmetry, such as those with the zinc-blende structure, the SO interaction is anisotropic and results in the effective existence of a momentum-dependent internal magnetic field capable of flipping spin states. Relaxation of spins in these systems is described well by the Dyakonov-Perel (DP) mechanism. Electron spins precess due to an effective magnetic field, until a scattering event takes place, after which the direction of the effective magnetic field changes. In this way, spins precess about randomly changing axes, and this leads to randomization of the spin average. In the strong scattering regime, $< \Omega > \tau_p \ll 1$, where $< \Omega >$ is the average spin precession frequency and τ_p is the momentum scattering time, the spin relaxation rate is proportional to τ_p [14],

$$\frac{1}{\tau} \propto \tau_p < \epsilon_F >^3, \tag{1.38}$$

For n-doped semiconductors above the MIT, the main source of spin relaxation is the DP mechanism [8]. At greater dopings, the hyperfine interaction mediates a very weak spin-flip scattering mechanism and provides a negligible relaxation rate compared to S-O relaxation mechanisms. At low doping concentrations, most charge carriers are localized at impurity sites and the hyperfine interaction is a very efficient spin relaxation channel.

Comparison between the strengths of the EY and DP mechanisms in n-doped semiconductors has been done in Ref. [15]. It has been found that in the non-degenerate regime

$$\frac{\tau_{s,EY}}{\tau_{s,DP}} \approx k_B T \tau_p^2. \tag{1.39}$$

Thus, the EY mechanism is said to be important at low temperatures and higher impurity densities.

The dominant momentum scattering mechanisms can be inferred from the temperature dependence of the mobility. For n-doped, III-V semiconductors, the relevant momentum scattering mechanisms are ionized impurity scattering (II) and longitudinal-optical-phonon scattering (LOP) [15]. For II scattering, using the Brooks-Herring formula for ionized impurity scattering of degenerate electrons, $\tau_p \approx \frac{T^{\frac{3}{2}}}{n_D}$ ($k_B T >> \epsilon_F$), and $\tau_p \approx T^0 n_D^0$ ($k_B T << \epsilon_F$). For LOP, although there is not a universal energy exponent, a dependence of $\tau_p \approx T^{-1}$ has been found to give the proper behavior of the mobility at high temperatures [6].

1.9 Hyperfine Effect

Nuclear spins can be polarized through the Zeeman interaction by external magnetic fields. Alternatively, nuclear spin polarization can result from the hyperfine interaction between nuclei and their surroundings. In GaAs, nuclear moments of the Ga and As isotopes undergo interactions with the electronic spin system, the lattice, and indirectly with the nuclear spin system itself. Nuclear moments can couple to the orbital angular momentum of electrons (chemical shift), or to the spin angular momentum (Knight shift). The chemical shift does not contribute significantly in systems with s-state electron orbits and in solid state systems where the orbital angular momentum is quenched by the lattice. The Knight field is a result of the hyperfine interaction between nuclear moments and s-band electron wavefunctions and mediates a second order coupling between nuclear moments through the electron spin system. This interaction is dominant in metallic systems at cryogenic temperatures where spin-phonon relaxation mechanisms are frozen out. By continuously pumping the electron spin system out of equilibrium, through electronic or optical means, it is possible to create large DNP. The exchange field acting on the electrons resulting from the nuclear spin system is called the Overhauser field

$$\mathbf{B_n} = f b_n \frac{< \mathbf{S} > \cdot (\mathbf{B} + \alpha < \mathbf{S} >)}{B^2 + \xi B_d^2} \mathbf{B}, \tag{1.40}$$

where b_n is the Overhauser field of the total nuclear polarization in GaAs, $\mathbf{B_e} = \alpha < \mathbf{S} >$ is the average electron field (the Knight field), ξ is the relative relaxation strength by the local dipole field B_d, and f is a leakage factor accounting for nuclear spin diffusion and other spin relaxation mechanisms [16].

When measuring τ_s, it is important to account for the existence of a B_n field. In Hanle measurements, B_n results in asymmetries and satellite peaks in the Hanle signal [17]. Thus, when using Hanle data to determine τ_s, B_n needs to be included in the model. However, modeling B_n requires more measurements to constrain the larger number of free parameters. Alternatively, one can suppress nuclear field effects by using an AC magnetic field to depolarize the nuclei and then ramping to the desired field value at a rate faster than the nuclei can polarize. In optical measurements this can also be done by light modulation, where the excitation light is alternated between left and right circular polarization at a rate faster than the rate at which nuclei can polarize.

Chapter 2

Device and Measurement Setup

2.1 Sample

The sample that was used for all measurements in this paper will now be discussed. The lateral spin valve was grown by layering GaAs with different doping values using molecular beam epitaxy (MBE). On top of an insulating GaAs substrate, a 500 nm undoped GaAs buffer layer was grown, followed by a 2.5 μm silicon doped n-GaAs channel layer. A doping level of $3 \times 10^{16}\text{cm}^{-3}$ was chosen in order to maximize the spin diffusion length, which occurs near the metal-insulator transition. For GaAs this occurs at $n \approx 2 \times 10^{16}\text{cm}^{-3}$. Next, in order to prevent the backflow of spin current and improve the injection efficiency, a Schottky barrier was created by adding another 30 nm GaAs layer with doping gradually increasing to about $5 \times 10^{18}\text{cm}^{-3}$. This was followed by a 5 nm Fe layer and capped by an Al/Au layer to prevent device oxidation.

Figure 2.2 shows a Keyence microscope image of the spin valve. The Fe contacts are in gray and Au cap layer in yellow. Delamination of the gold contacts is due to excess sonication in the liftoff step of fabrication.

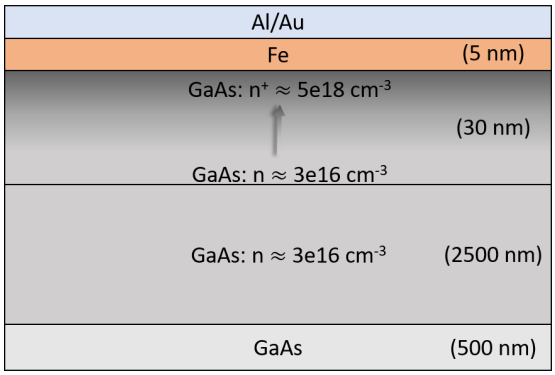

Figure 2.1: Diagram of an Fe/n-GaAs heterostructure.

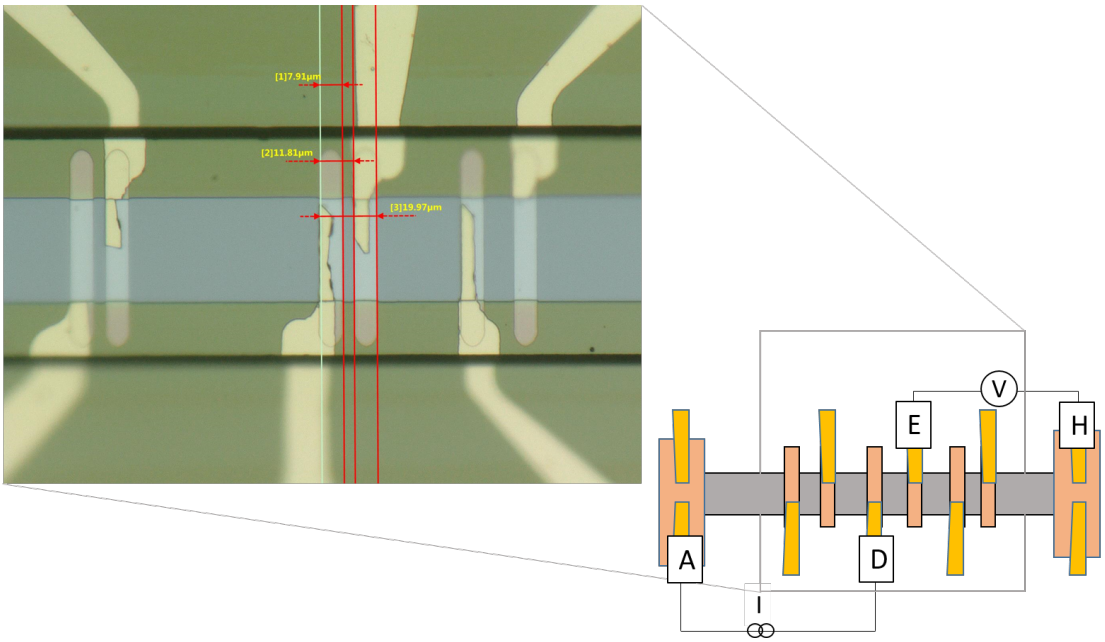

Figure 2.2: Keyence microscope image of an Fe/n-GaAs NLSV. The cartoon indicates the contacts used for spin injection and non-local detection. Injector, detector contact and separation widths are 7.91 μm, 3.90 μm, and 8.16 μm, respectively. GaAs, Fe, and Au are represented by gray, pink, and yellow, respectively.

2.2 Charge Transport

Figure 2.3 below shows charge transport data for the Fe/n-GaAs sample as a function of temperature. Magnetotransport measurements were used to obtain resistivity and carrier concentrations at various temperatures.

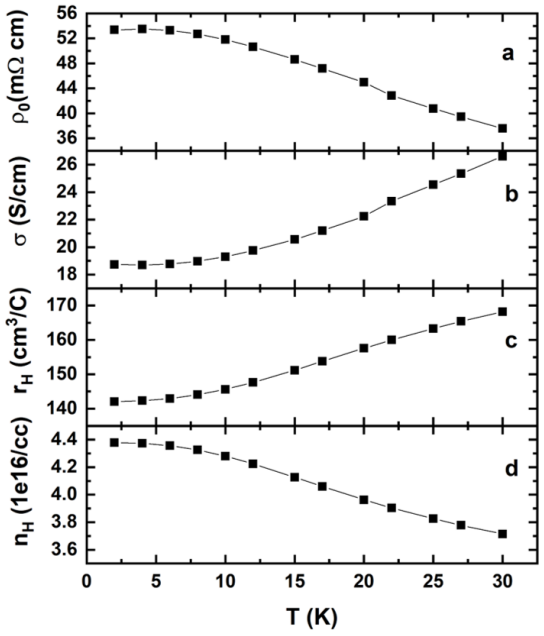

Figure 2.3: Charge transport data for Fe/n-GaAs as a function of temperature. (a) resistivity (b) conductivity (c) Hall factor and (d) Hall concentration are shown as solid black points.

Figure 2.4 shows low temperature resistivity and carrier density results (red) along with higher temperature data obtained from a different cool down (black). The increase in the carrier concentration below 50 K is likely due to the Hall measurement scheme. The actual carrier concentration is expected to remain around the value at 50 K.

Figure 2.5 shows the Hall mobility over a wide range of temperatures. The dominant momentum scattering mechanism can be inferred from the temperature dependence of

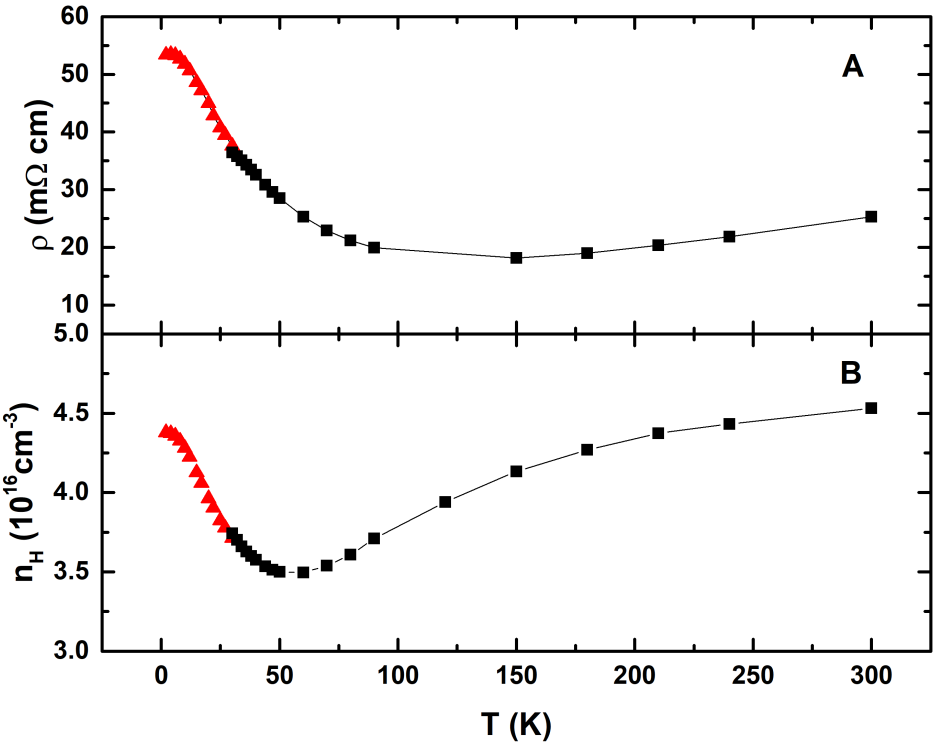

Figure 2.4: Charge transport properties for an Fe/n-GaAs sample as a function of temperature. (A) resistivity (B) Carrier density. Black squares indicate data from a different cool down.

the mobility. Below 100 K, the mobility appears to be largely dominated by II scattering.

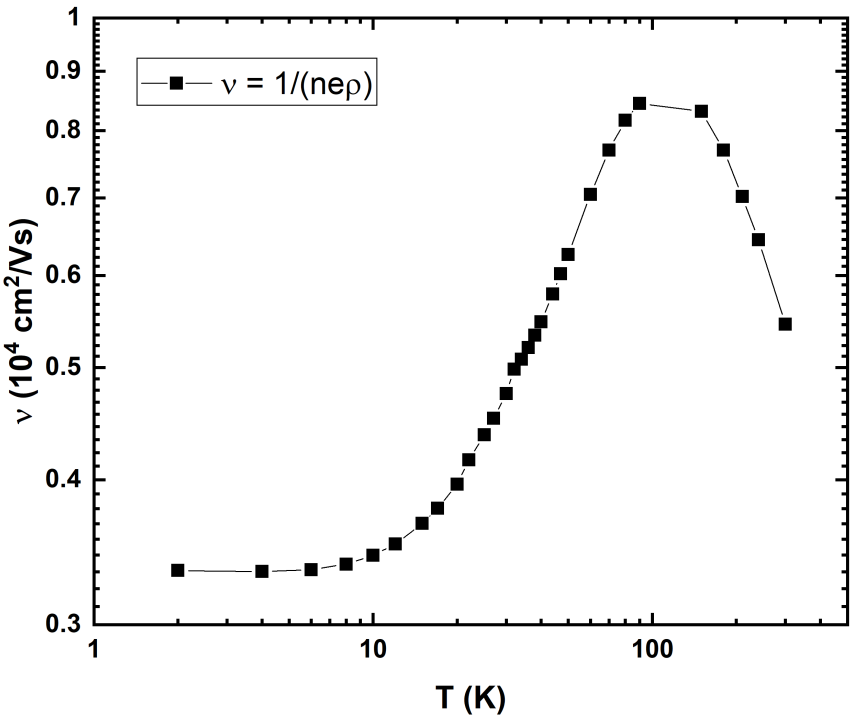

Figure 2.5: Mobility determined from resistivity and Hall density.

2.3 Setup

The sample was cooled down to a base temperature of 2 K using a Quantum Design Physical Properties Measurement System (PPMS). The PPMS applies magnetic fields using a superconducting magnet. In-plane and out-of-plane fields were applied by rotating the sample holder inside the PPMS dewar. Automation of experiments was achieved using a GPIB to connect a Keithley 220 programmable current source, 2182 Nanovoltmeter, and 7001 Switch System to the measurement computer, as shown in Figure 2.6. Interfacing to the measurement devices and the PPMS was done using LabVIEW software.

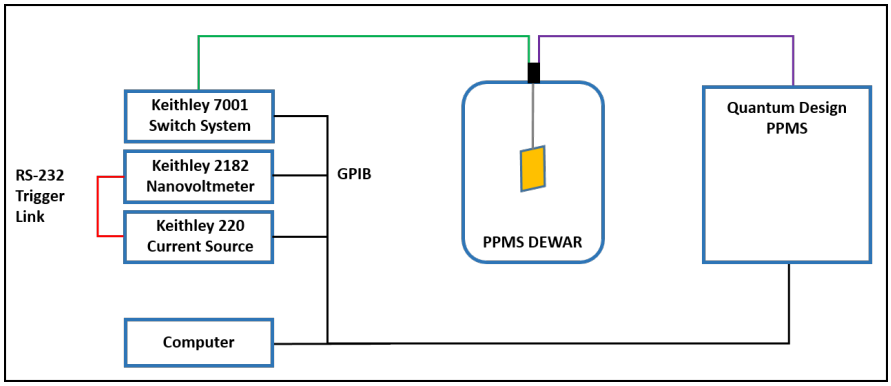

Figure 2.6: Measurement setup.

2.4 NLSV Measurement

DC NLSV measurements were performed to obtain baseline results for comparison. For DC NLSV measurements, spin injection was done using a 1 mA current applied to the Fe contacts A and D (Figure 2.2). Measurement of the residual polarization 3.90 μm outside of the current path was done by measuring the voltage difference between contacts E and H. The NLSV voltage signal was obtained by sweeping an in-plane magnetic field, B_y, allowing 4 seconds for field ramping, and repeating voltage measurements for averaging.

Figure 2.7 shows raw voltage data obtained at 30 K for a forward and backward sweep.

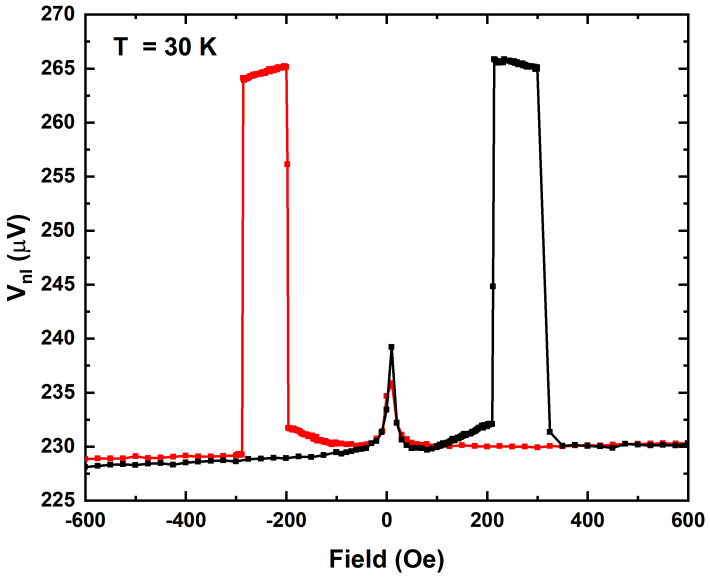

Figure 2.7: Raw NLSV signal.

A linear background was subtracted off (due to a weak planar Hall effect) using a linear fit to the signal, excluding the switching window voltage data. Averaging was performed at each measurement point to reduce background signal noise. This was repeated for temperatures between 2 K and 30 K, and the results are shown in Figure 2.8. The center peak that results from DNP in the NLSV signal can be understood as follows: when the external field switches direction at zero field, the nuclear field lags and causes precession of spins and a reduction of the signal. Note that complete spin decoherence would correspond to a value that is half of the maximum measured V_{nl}.

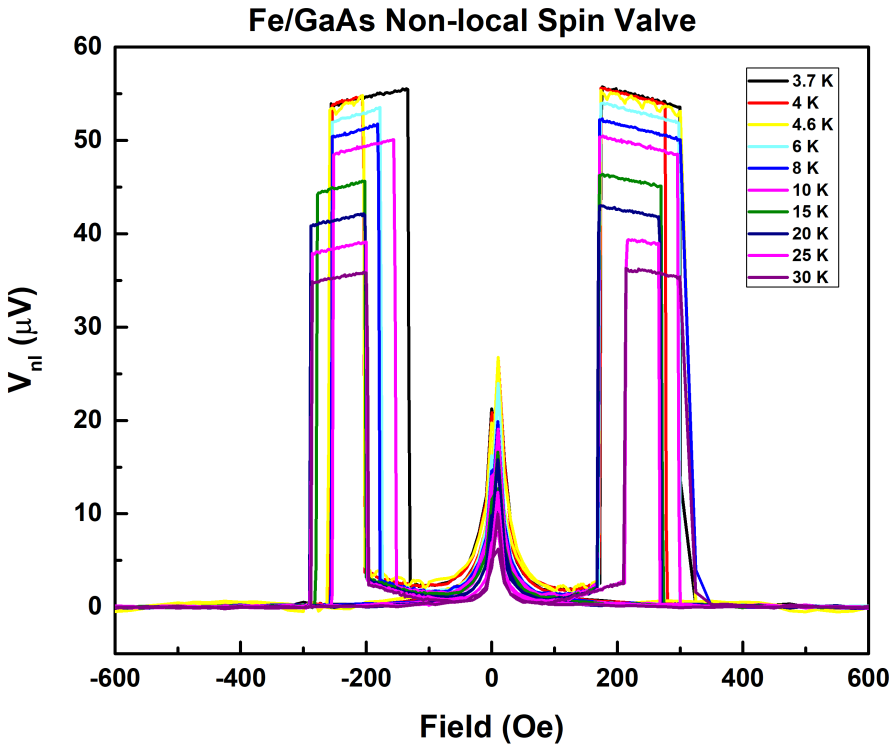

Figure 2.8: DC NLSV signal between 2 K and 30 K.

2.5 Hanle Measurement

DC Hanle baseline measurements were performed in the same manner as NLSV, except that the sample was rotated so that the magnetic field was perpendicular to the sample plane. Figure 2.9 shows Hanle signals at 30 K for different relative orientations of the injector and detector. The complete Hanle signal is obtained by subtracting the perpendicular signal component from the parallel one, eliminating the background.

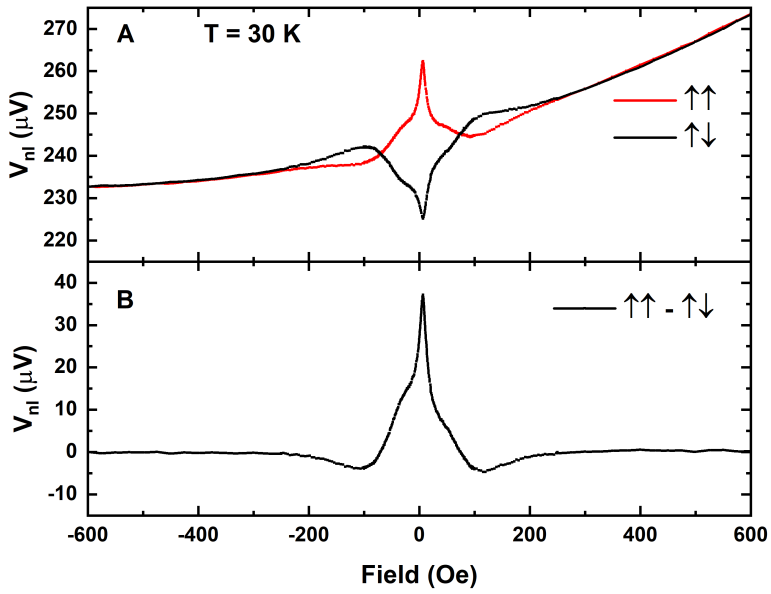

Figure 2.9: Raw DC Hanle voltage for both FM contact orientations (A) and the difference (B).

During Hanle measurements, the spin lifetime is influenced by a combination of the mechanisms mentioned in section 2.2. At cryogenic temperatures, the hyperfine coupling tends to make Hanle spin lifetime measurements difficult. The Overhauser field, resulting from nuclear polarization, can point either parallel or anti-parallel to the applied external field. For field ramping faster than the nuclear system equilibration time, the Overhauser field will lag its steady state value, causing an asymmetry in the spin signal as one sweeps across zero-field.

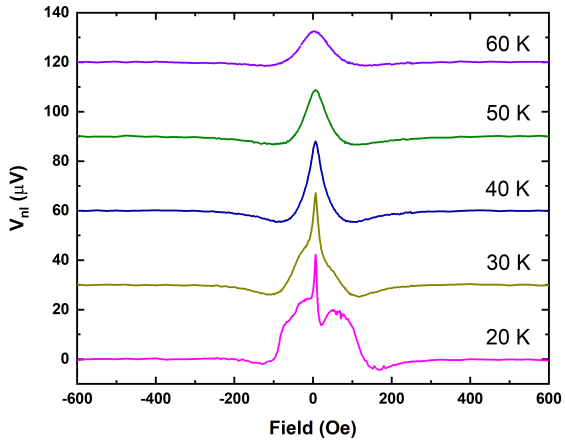

Figure 2.10: Non-local spin accumulation at detector a distance of 3.90 μm from the injector with an applied current of 1 mA and an out-of-plane magnetic field. 4 seconds passed between each data point to allow the magnetic field to sweep. Hyperfine effects noticeably begin to distort signal below 40 K.

For systems where the nuclear polarization becomes significant, Hanle curves contain additional maxima besides the center peak, corresponding to compensation of the external field by $\mathbf{B_n}$. For external fields completely perpendicular to the spin flow, the peaks are symmetrically centered around the central peak. Around $B = 0$, even very weak external magnetic fields result in significant nuclear polarization, which results in electron spin depolarization. The sharp fall in the polarization peak near $B = 0$ is due to the large amplification factor of the nuclear field. Figure 2.10 shows Hanle spin signals at different temperatures. Hyperfine effects become noticeable below 30 K where "pinching" of the signal peak and slight asymmetry occurs. This asymmetry becomes more visible at 20 K as well as the emergence of two more maxima. The misalignment of the magnetic field and the true normal of the spin valve was less than 1 degree, resulting in the appearance of asymmetries.

2.6 Pulsed injection current Setup

Spin relaxation in the electronic and nuclear systems vary in time scales. Nuclear relaxation through the lattice occurs on the order of seconds, or much greater, while electron system spin relaxation occurs on the order of nanoseconds. A pump-probe measurement technique uses this fact to independently probe the spin dynamics of the electronic system without allowing the nuclear system to polarize through DNP. This way, any hyperfine effects would be removed from voltage measurements.

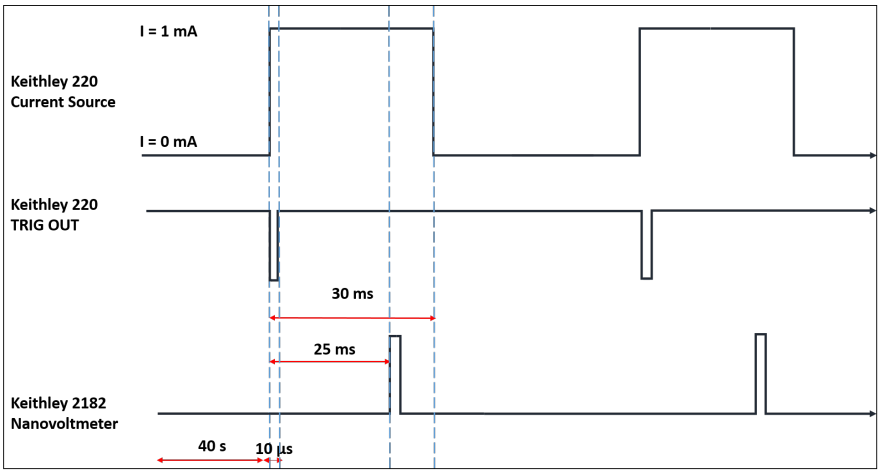

Figure 2.11: Pulse-probe timing diagram utilized for spin valve and Hanle measurements.

For the following pulsed NLSV and Hanle measurements, hyperfine effects were reduced as shown in Figure 2.11. First the injection current is turned off for 40 seconds to allow any non-equilibrium nuclear polarization to decay via spin-lattice relaxation. Then, a 30 ms, 1 mA current pulse is applied such that the nuclear spin system does not have time to polarize significantly, probing only the electronic spin system. At the beginning of this current pulse, the Keithley 220 sends a trigger signal to the Keithley 2182 nanovoltmeter. The nanovoltmeter then waits 25 ms before making the measurement. The wait time required for hyperfine removal was determined using the lowest temperature data, as the wait time required for the decay of nuclear system polarization increases

with decreasing temperature. In our sample, a 10 second wait time was sufficient for hyperfine signal suppresion at 60 K, whereas 30 seconds was required at 2 K for similar results. Many voltage measurements were averaged for DC spin valve and Hanle data to improve the signal to noise ratio. Pump-probe measurements were not averaged and therefore show a greater background noise signal.

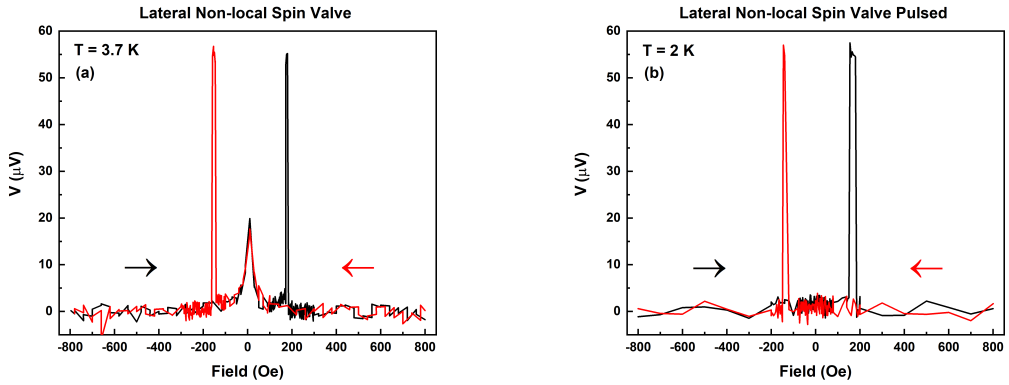

Figure 2.12: GaAs Non-local spin valve. (a) A 1 mA current was applied to inject spin current into the semiconductor. $\rightarrow$ and $\leftarrow$ indicate negative to positive sweeping direction and vice-versa. The zero-field peak illustrates presence of hyperfine effect at low temperatures. (b) Demonstration of hyperfine signal removal in an Fe/n-GaAs spin valve near 2 K using the pump-probe method. The density of field points was increased near zero field to ensure no noticeable hyperfine signal.

Figure 2.12 demonstrates removal of hyperfine effects from spin valve data around 2 K. Figure 2.12(a) shows the DC Hanle signal at 3.7 K due to the DC current causing sample heating, preventing the PPMS to cool down to 2 K . The pulsed signal was able to remain at 2 K. For temperatures above 3.7 K, both DC and pulsed measurements were able to achieve the desired temperature. At low temperatures the switching window width tends to shrink, as well as vary for each cool down. Having shown removal of hyperfine effects around 2 K using this approach, Hanle data at higher temperatures can be similarly acquired and analyzed accurately to determine D and τ_s.

Chapter 3

Data and Analysis

3.1 NLSV Signal vs T

NLSV data were obtained at temperatures between 2 K and 30 K using both DC and pulsed measurements, shown in Figure 3.1. A linear background subtraction was done to remove Hall effects. Unlike the DC data, pulsed measurements were not averaged, resulting in a greater noise.

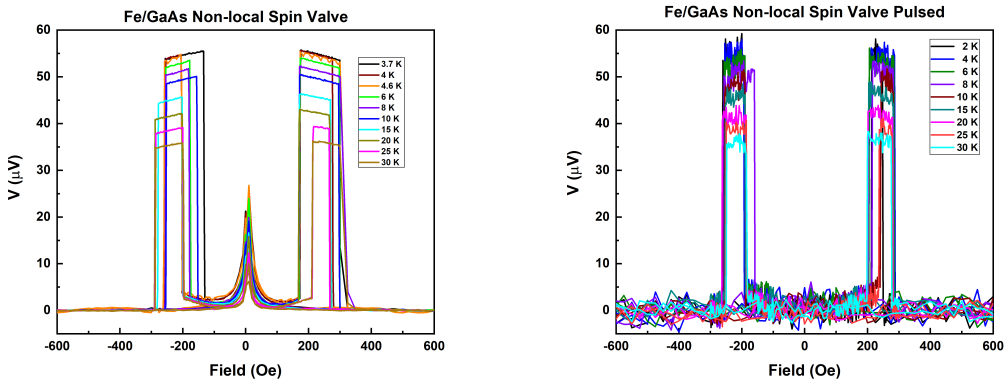

Figure 3.1: Non-local spin valve signal. (A) DC current bias applied at temperatures between 2 K and 30 K. (B) Signal after removal of nuclear spin magnetization using pulse-probe technique.

Figure 3.2 shows the switching window peak voltage for both sweeping directions. Pulsed

signal values near zero-field are comparable to background noise, indicating suppression of hyperfine effects.

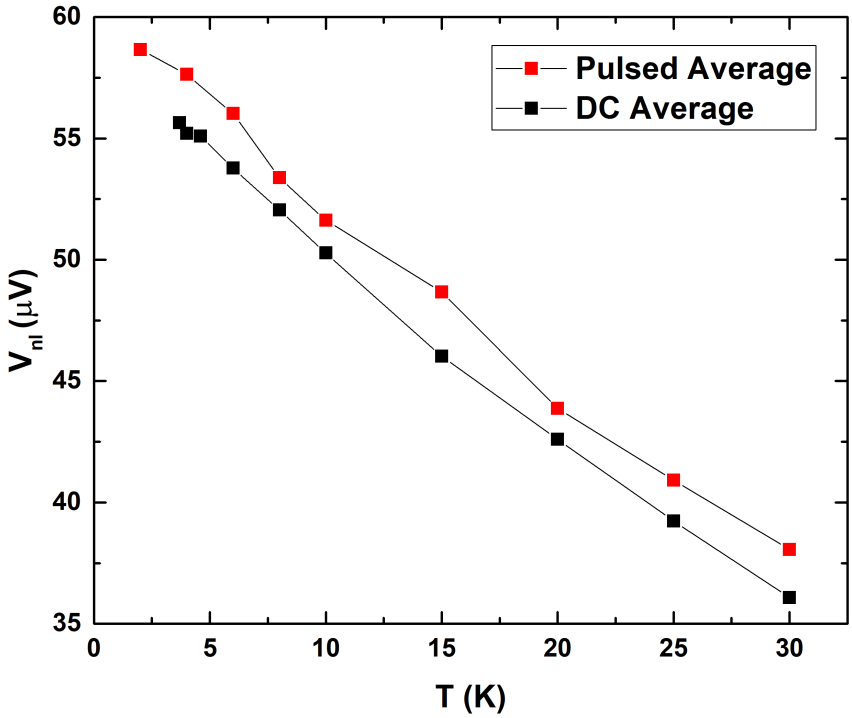

Figure 3.2: NLSV window peak voltage vs T. Data shows the average of left and right sweep direction peak voltages, done for both pulsed and dc measurements.

3.2 Hanle Signal vs T

Hanle measurements were done for temperatures below 60 K using both DC and pulsed current sources. Figure 3.3 shows Hanle curves at 2 K and 30 K. Background signal removal is done by subtracting the voltage signal with contacts anti-parallel from the voltage with contacts parallel.

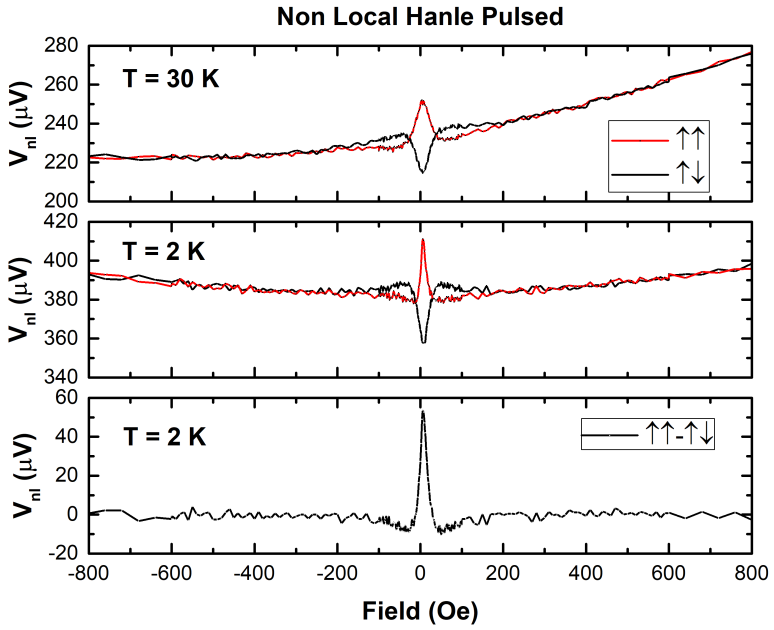

Figure 3.3: Pulsed Hanle data along with background Hall signal.

With a decrease in temperature, the peak signal increases, as shown in Figure 3.4, indicating an increase in spin polarization at the detector. Also visible is the narrowing of the linewidth, which is approximately inversely proportional to the spin lifetime.

The polarization, which is proportional to measured non-local voltage, appears to decrease linearly with increasing temperature (Figure 3.2), consistent with previous experiments [8].

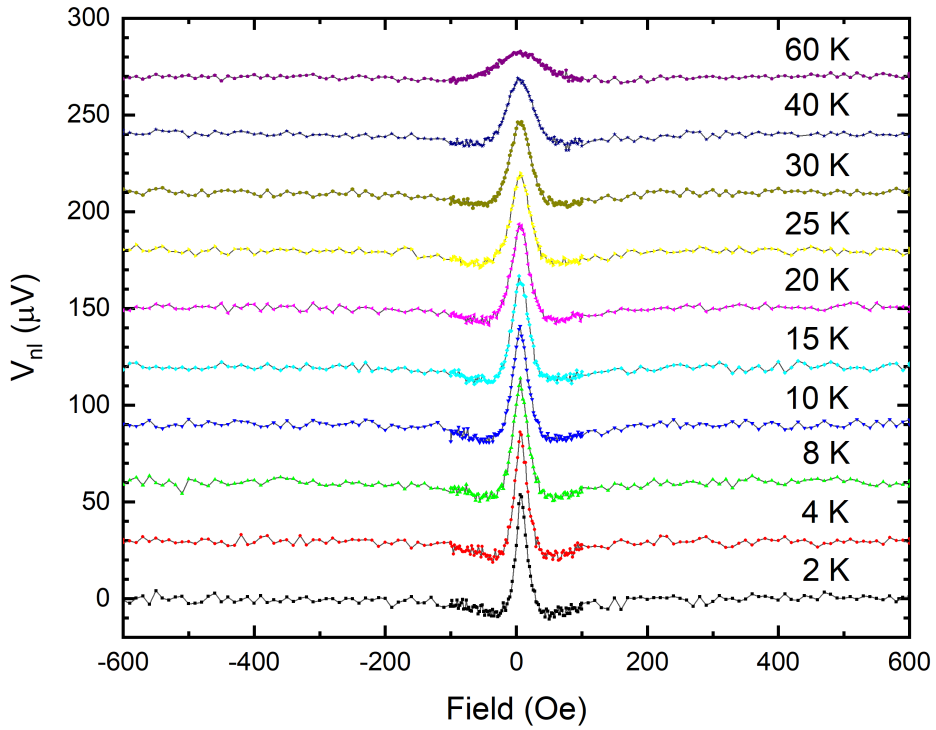

Figure 3.4: Hanle signal at various temperatures with hyperfine contribution removed. The data are plotted with a constant offset between each curve.

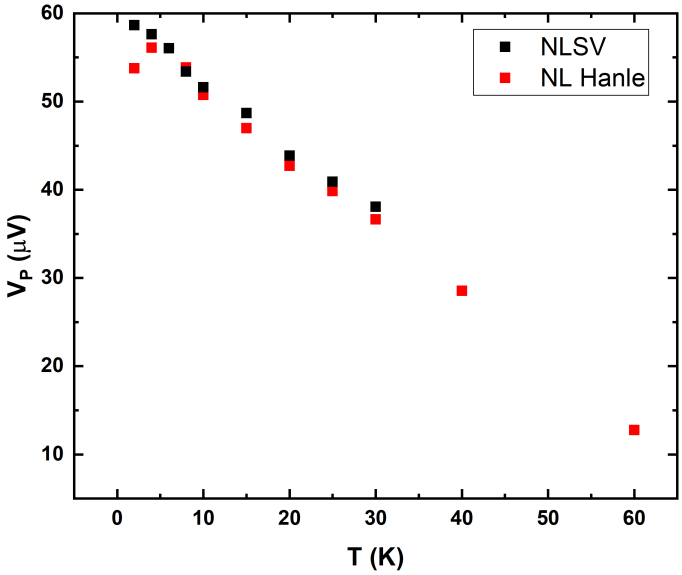

Figure 3.5: Peak non-local voltage signal from pulsed Hanle and pulsed NLSV measurements.

3.3 Spin Lifetime Extraction

Due to the spatial extent of the GaAs spin channel, the diffusion can be approximated as 1D in the x direction. Spin lifetimes at varying temperatures were obtained by fitting Hanle data to Equation 1.25 after integrating over all possible separation distances between injector and detector contacts

$$V_{nl} \propto \int_{-w_{FM}^{inj}}^{0} \int_{d}^{d+w_{FM}^{det}} \sqrt{\frac{D\tau_s}{1+2\pi i\gamma_e(H-H_0)\tau_s}} e^{-(x_{inj}-x_{det})\sqrt{\frac{1+2\pi i\gamma_e(H-H_0)\tau_s}{D\tau_s}}} dx_{det}dx_{inj}. \tag{3.1}$$

Fits to Equation 3.1 with τ_s and D as free parameters are shown in Figure 3.6 . Fitting was done using data from the interval [-200 , 200] Oe. The center of the Hanle peak was allowed to vary, which usually resulted in a magnetic field shift of 5-8 Oe. This is due to trapped flux in the superconducting magnet, which varies between runs.

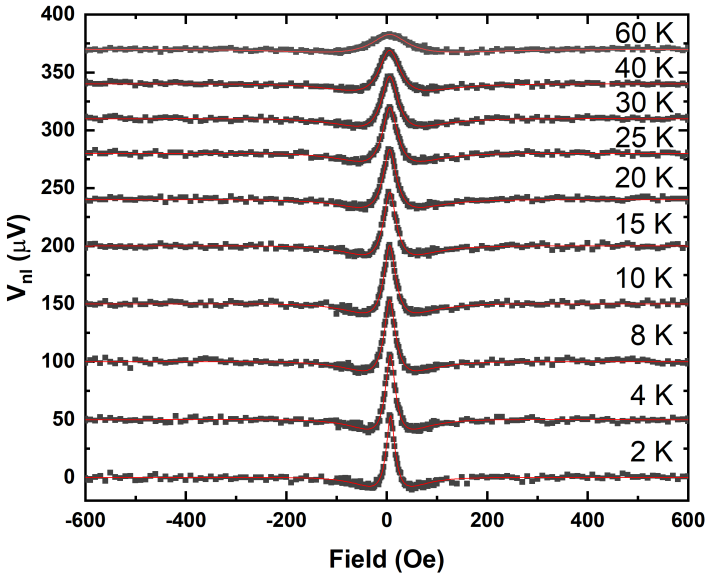

Figure 3.6: Hanle fits to Equation 3.1 for τ_s and D.

To constrain the fitting, the diffusion coefficient was also determined from the Hall mobility using Equation 1.32. The Fermi energy was determined assuming a parabolic energy dispersion relation, the electron carrier density and mobility obtained from transport measurements, and the effective electron mass in GaAs. The carrier density value at 50 K was used for temperatures below 50 K.

As a check, D was compared to its theoretical low and high temperature limits. Figure 3.7 shows D calculated using Equation 1.32 along with these limits. Theoretically, the values determined from Equation 1.32 (black squares) should connect the blue and magenta lines. At high temperatures, D does approach the high temperature behavior.

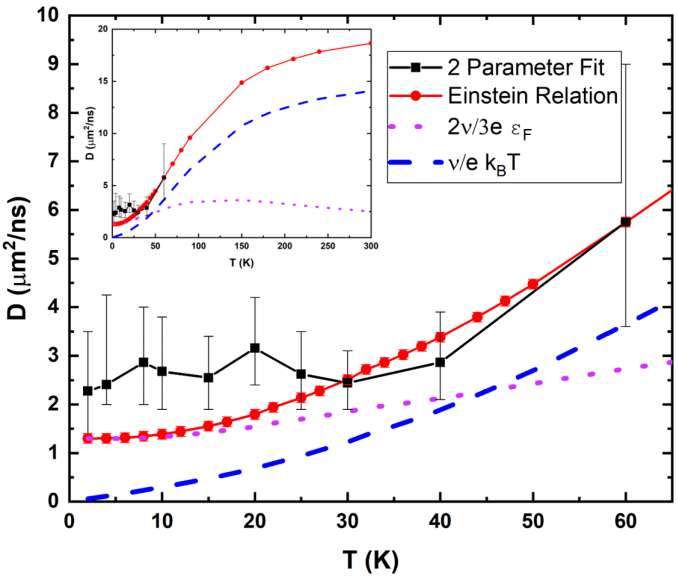

Figure 3.7: Diffusion coefficient determined from Equation 1.32 (red), 2 parameter fit to Equation 1.25 (black), and low (magenta) and high (blue) temperature limits.

D values extracted from Equation 1.32 were then used in the Hanle fitting to extract τ_s. These fits are shown in Figure 3.8.

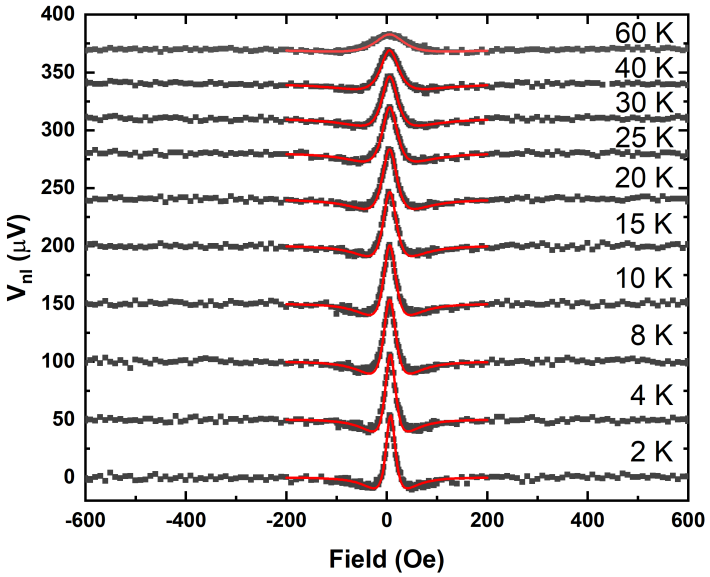

Figure 3.8: Fitting of Equation 1.25 using D from the Einstein relation.

Figure 3.9 shows the behavior of the spin lifetime below 60 K. The two different methods of obtaining τ_s agree within error limits.

The mobility ν is often used to determine the momentum scattering sources. ν was determined from Hall measurements and was fit to II and LOP scattering, adding the scattering rates using Matthiessen's rule

$$\nu^{-1} = (A + BT^{\frac{3}{2}})^{-1} + (CT^{-1})^{-1}, \tag{3.2}$$

where A accounts for the spin degeneracy at low temperatures and B and C are fitting parameters. Figure 3.10 shows the results with A = 3.8 x 10^3 cm^2 V^{-1}s^{-1}, B = 13 cm^2 V^{-1}s^{-1}K$^{-\frac{3}{2}}$, and C = 1.78 x 10^6 cm^2 V^{-1}s^{-1}K^{-1}. Between 10 K and 100 K, II scattering appears to dominate. Below 10 K, ν becomes temperature independent as all scattering rates approach a constant as $T \to 0$

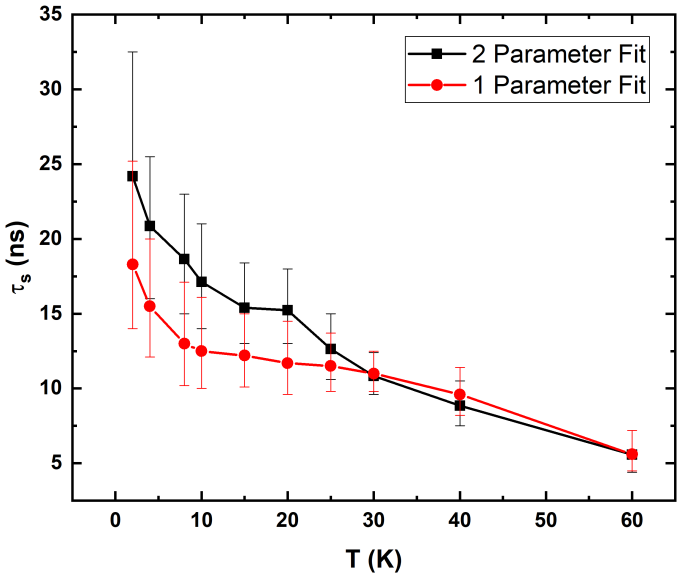

Figure 3.9: Spin lifetime obtained from pulsed Hanle measurements using a 2 parameter fit model (black) and constrained model (red).

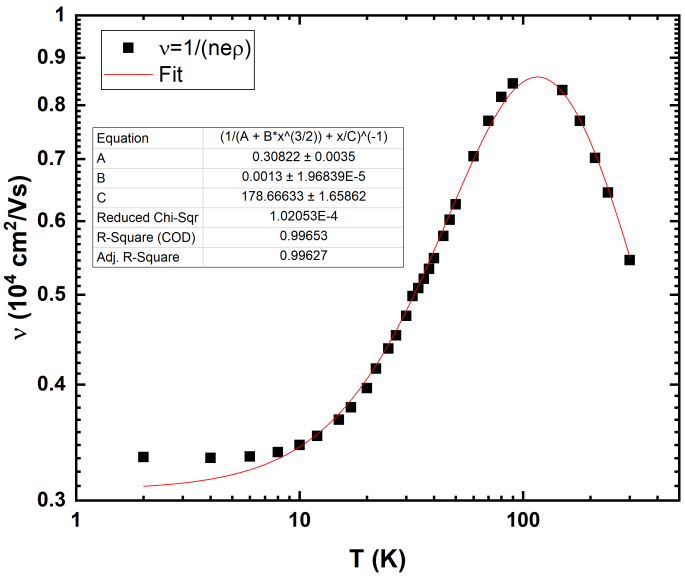

Figure 3.10: Carrier mobility fit to Equation 3.2.

Chapter 4

Discussion

The purpose of this work was to study electron spin lifetimes in n-GaAs at temperatures below 40 K. The electron spin polarization signal size and spin lifetime are important parameters in the study of FM/III-V semiconductor heterostructures. It has been found that for n-GaAs doped near the MIT DP theory does not predict τ_s well below T = 40 K [5] [6] [8]. A possible reason for this could be that DNP effects become more significant at lower temperatures, leading to errors when measuring τ_s. DNP effects manifest themselves in added signal satellite peaks and the widening of the Hanle curves. Thus, not removing or accounting for these effects when modeling the spin signal will result in smaller spin lifetimes.

4.1 DNP Removal

The effectiveness in removing hyperfine interaction effects from Hanle and NLSV measurements by current pulsing was determined qualitatively. Hyperfine effects are particularly noticeable in oblique Hanle measurements, where significant shape distortions, including satellite peaks, will form even at small oblique angles. This effect becomes larger at lower temperatures, as seen in Figure 2.10. Based on the Hanle lineshapes around $\mathbf{B} = 0$ and the success of the fitting without accounting for hyperfine effects, it is suggestive that this effect was suppressed. Figures 3.6 and 3.8 show noticeably different quality of fits near $\mathbf{B} = 0$. Below 30 K, the single parameter fits appears to

dip lower, fitting the data better. However, the fitted curve is somewhat narrower than the data. Hyperfine effects would result in the measured Hanle data to be wider lead to overestimation of τ_s values.

4.2 Spin Lifetime in GaAs

In determining τ_s, the 1D lateral drift-diffusion model was used. In order for this approximation to be valid, λ_s needs to be greater than the channel thickness otherwise the diffusion will decay faster than an exponential. Figure 4.1 shows λ_s determined from single and 2 parameter fitting to the 1D latteral drift diffusion model (Equation 1.20). λ_s appears to be 2-3x larger than the channel thickness for temperatures below 30 K.

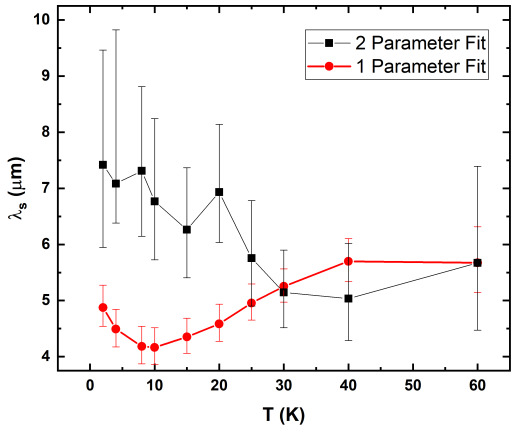

Figure 4.1: Spin diffusion lengths, $\lambda_s = \sqrt{D\tau_s}$ calculated using D and τ_s determined from both the single and 2 parameter fitting.

As the doping concentration changes so does the Fermi energy and the temperature that separates the degenerate and non-degenerate regimes. At a doping of 3.5 x 10^{16} cm^{-1}, $T_F \approx 70\ K$. Thus, measurements in this work would fall in the transition between the degenerate and non-degenerate regime. In the non-degenerate regime, DP relaxation due to II scattering, which was shown to be the dominant momentum scattering

mechanism for T below 100 K, $\lambda_s = \sqrt{D\tau_s} \propto \sqrt{\nu k_B T T^{-\frac{9}{2}}} \propto \sqrt{\tau_p k_B T T^{-\frac{9}{2}}} \propto T^{-1}$. In the degenerate regime however, $\lambda_s \propto \sqrt{\nu\tau_s} \propto \sqrt{\tau_p \tau_p^{-1}}$ and λ_s is expected to be nearly temperature independent. We observe λ_s does not seem to vary significantly ($\approx 20\%$), especially considering that between 2 K and 40 K both D and τ_s vary as much as by a factor of 2.

The τ_s values obtained from the 1-parameter and 2-parameter fitting, shown in Figure 3.9, are in good agreement and indicate τ_s continues to increase with decreasing temperature. However, the rate at which τ_s increases seems to vary. The temperature dependence of the spin relaxation rate τ_s^{-1} can provide insight into the underlying spin relaxation mechanisms. Figure 4.2 shows the temperature dependence of the spin relaxation rate.

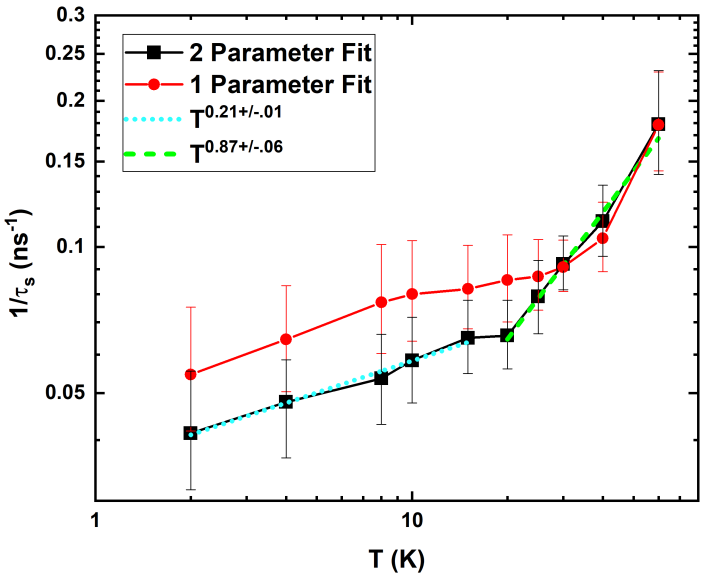

Figure 4.2: Spin relaxation rate variance with temperature.

Despite the offset below 30 K, both single and 2 parameter fit values seem to exhibit

similar temperature dependence. τ_s^{-1} values extracted from the 2 parameter Hanle fitting were fit by a line and show different temperature dependences below and above 20 K. At temperatures greater than 20 K, spin lifetimes are approximately inversely proportional to the temperature. This type of temperature dependence is not consistent with DP relaxation. For degenerate electrons, DP predicts the spin lifetime will eventually plateau. This is illustrated by Figure 2.5, which shows the mobility as a function of temperature. At low temperatures, $\nu \propto \tau_p$ becomes temperature independent and $\tau_s^{-1} \propto \tau_p$ should reach a limiting value.

Figure 4.4 compares τ_s values obtained from different n-GaAs NLSV heterostructures. τ_s values plotted as black squares are from NLSV measurements at various injector-detector separations, where the decay of the voltage signal amplitude was fit by numerically solving the 2D version of Equation 1.16 [6]. The blue star and cyan circle data were obtained by fitting Equation 1.16 to pulsed non-local Hanle data [8]. In both [8][6], τ_s was succesfully modeled by DP theory for temperatures above 60 K. Below 60 K, τ_s is smaller than the predicted values. τ_s values obtained in this current work for T between 30 K - 60 K are in excellent agreement with those found in other measurements. At 30 K, however, variations in the measured τ_s appear. This could be due to differences in doping as τ_s agrees well with the Co_2MnSi/n-GaAs data which has approximately the same doping as in this work. Still, if the difference in τ_s was just due to doping, then the difference between the two Fe/n-GaAs τ_s values at T = 30 K would be larger. Large τ_s values obtained from the NLSV measurements (black squares) generally agree with other τ_s measurements on n-GaAs near the MIT [18]. Resonant spin amplification experiments by Kikkawa and Awschalom [5] on $n = 1 \times 10^{16}$ cm^{-1} doped GaAs reported $\tau_s \approx 100$ ns at T = 10 K. These experiments were done by using polarized light pulses to establish and detect spin polarization.

A possible explanation for the different τ_s in Figure 4.4 could be the orientation of the applied magnetic field. In Hanle measurements, an out-of-plane B field is applied to induce spin precession and τ_s is determined from the width of the polarization signal. Precession, however, could be induced by any B field perpendicular to the spin polarization. The existence of inhomogeneous nuclear fields [8] could cause the width of the

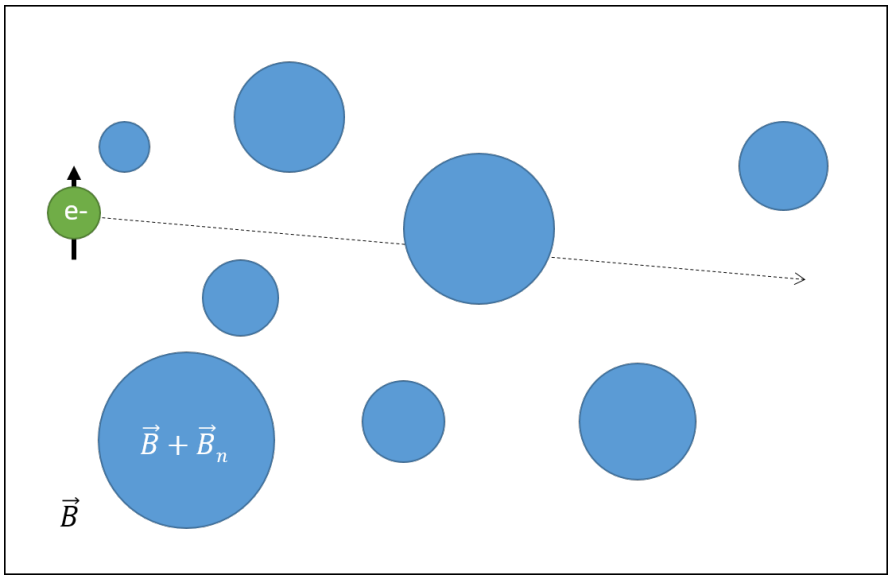

Figure 4.3: Cartoon of inhomogeneous nuclear environment. Enhanced electron-nuclear interaction occurs near donor sites.

Hanle curve to broaden, resulting in shorter (effective) spin lifetimes τ_s^*. Spin valve measurements rely on an in-plane B field to probe the chemical potential of each spin band. They do not rely on precession and hence τ_s is less susceptible to relaxation by inhomogenous nuclear fields.

To conclude, a pump-probe technique was used to measure spin polarization in NLSV and Hanle experiments. The pulsed NLSV results indicate that the spin polarization signal in NLSV measurements is sensitive to nuclear polarization. This result implies that when extracting τ_s from NLSV measurements, DNP must be removed or included in the modeling. τ_s results obtained from 1-paramter and 2-parameter fitting of Hanle data are in good agreement with each other as well as with previous τ_s measurements at similar doping. τ_s values extracted from Hanle measurements were found to differ with τ_s values determined from NLSV measurements and for T below 40 K. This result could in part be due to the doping differences between the samples. Another possible factor could be that shorter τ_s are inherent in measurements that require out-of-plane fields to induce spin precession. This explanation is consistent with the agreement of

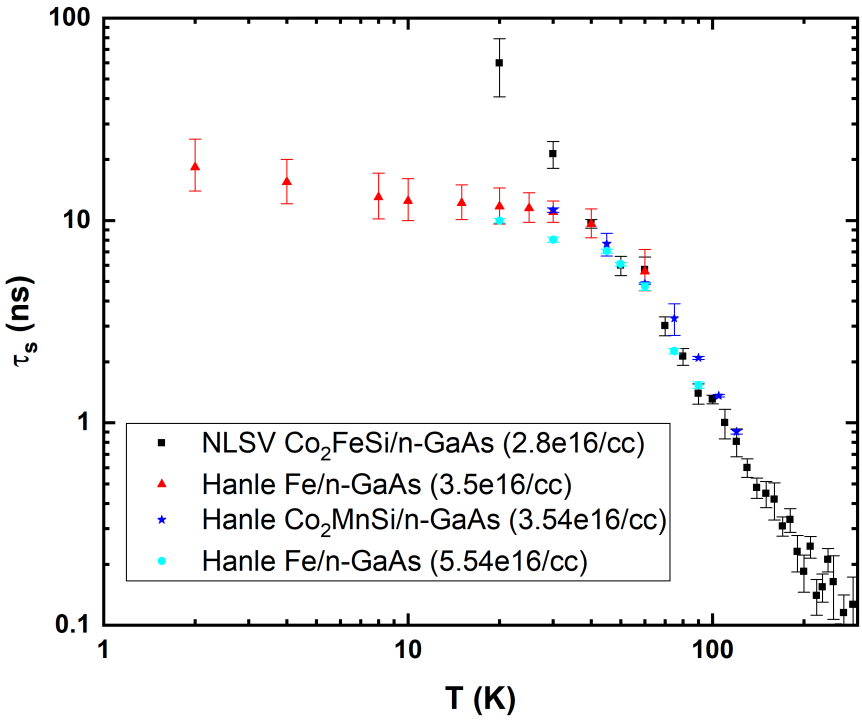

Figure 4.4: τ_s obtained in different n-GaAs lateral NLSV heterostructures. Red triangles are from the single-parameter fitting.

τ_s values obtained using either in-plane and out-of-plane fields. Lastly, the ability to fully eliminate DNP using the current pump-probe setup is questionable. NLSV and Hanle measurements indicate that nuclear polarization signatures were significantly attenuated at all temperatures. However, because τ_s values obtained were significantly lower than expected, DNP might still be present. Alternatively, lower τ_s could be due to inhomogenous nuclear fields causing broadening of the Hanle signal. To be more certain, oblique Hanle measurements should be performed to detect any DNP features. τ_s for temperatures below 20 K could also be measured from NLSV and compared to oblique Hanle results to address if τ_s differences are due to the measurement technique used.

Bibliography

[1]R. Meservey and P. M. Tedrow, "Spin-polarized electron tunneling", Physics Reports **238**, 173–243 (1994).

[2]M. Julliere, "Tunneling between ferromagnetic films", Physics Letters A **54**, 225–226 (1975).

[3]M. Johnson and R. H. Silsbee, "Interfacial charge-spin coupling: injection and detection of spin magnetization in metals", Physical review letters **55** (1985).

[4]E. Hirota, *Giant magneto-resistance devices* (Springer Berlin Heidelberg, Berlin, Heidelberg, 2002).

[5]J. M. Kikkawa and D. D. Awschalom, "Resonant spin amplification in n-type GaAs", Physical Review Letters **80**, 4313–4316 (1998).

[6]T. A. Peterson, S. J. Patel, C. C. Geppert, K. D. Christie, A. Rath, D. Pennachio, M. E. Flatté, P. M. Voyles, C. J. Palmstrom, and P. A. Crowell, "Spin injection and detection up to room temperature in Heusler alloy/n-GaAs spin valves", Physical Review B **94**, 235309 (2016).

[7]P. H. Song and K. W. Kim, "Spin relaxation of conduction electrons in bulk III-V semiconductors", Phys. Rev. B **66**, 035207 (2002).

[8]C. C. Geppert, "Spin-dependent transport phenomena in ferromagnet/semiconductor heterostructures", PhD thesis (2014).

[9]D. J. Monsma, J. C. Lodder, T. J. A. Popma, and B. Dieny, "Perpendicular hot electron spin-valve effect in a new magnetic field sensor: the spin-valve transistor", Physical review letters **74** (1995).

[10]P. Chuang, S.-C. Ho, L. W. Smith, F. Sfigakis, M. Pepper, C.-H. Chen, J.-C. Fan, J. P. Griffiths, I. Farrer, H. E. Beere, G. A. C. Jones, D. A. Ritchie, and T.-M. Chen, "All-electric all-semiconductor spin field-effect transistors", Nature nanotechnology **10**, 35–39 (2015).

[11]Z. G. Yu and M. E. Flatté, "Spin diffusion and injection in semiconductor structures: electric field effects", Phys. Rev. B **66**, 235302 (2002).

[12]R. A. Smith and R. L. Sproull, "Semiconductors", Physics Today **13**, 50–50 (1960).

[13]D. Kolbl, "Spins, disorder and interactions in gaas and graphene", PhD thesis (2018).

[14]P. Boross, B. Dóra, A. Kiss, and F. Simon, "A unified theory of spin-relaxation due to spin-orbit coupling in metals and semiconductors", Scientific Reports **3** (2013).

[15]M. Wu, J. Jiang, and M. Weng, "Spin dynamics in semiconductors", Physics Reports **493**, 61–236 (2010).

[16]A. Overhauser, "Polarization of nuclei in metals", Physical Review **92**, 411–415 (1953).

[17]M. K. Chan, "Hyperfine effects in ferromagnet-semiconductor heterostructure", PhD thesis (2010).

[18]R. I. Dzhioev, K. V. Kavokin, V. L. Korenev, M. V. Lazarev, B. Y. Meltser, M. N. Stepanova, B. P. Zakharchenya, D. Gammon, and D. S. Katzer, "Low-temperature spin relaxation in n-type GaAs", Phys. Rev. B **66**, 245204 (2002).